Spring 2015

Physical Properties of Iron Oxide Nanoparticles

Nicklaus Carter
The University of Maine

PHYSICAL PROPERTIES OF IRON OXIDE NANOPARTICLES

By

Nicklaus Carter

A Thesis Submitted in Partial Fulfillment
Of the Requirements for a Degree with Honors
(Bioengineering)

The Honors College

University of Maine

May 2015

Advisory Committee:
  Michael D. Mason, Ph. D, Professor of Bioengineering, Advisor
  Sara L. Walton, Ph.D, Professor of Bioengineering
  William J. DeSisto, Ph.D, Professor of Chemical Engineering
  Robert W. Meulenberg, Ph. D, Associate Professor of Physics and LASST
  Sarah Harlan-Haughey, Ph. D, Professor of English and Honors

ABSTRACT:

Magnetic Resonance Imaging (MRI) relies heavily on contrast agents such that diagnosis of various diseases can be made with increased confidence. Current contrast agents for MRI depend on various chelated molecules composed of a toxic gadolinium ion, Gd^{3+}. In 2006, a discovery was made connecting Nephrogenic Systemic Fibrosis (NSF) and these gadolinium based contrast agents (GBCAs). The connection between life threatening NSF and GBCAs stems from patients with pre-existing kidney malfunctions. It has been proposed that an alternative agent such as iron oxide nanoparticles (IONPs) be investigated. These IONPs theoretically will have similar responses in efficiency of improving the contrast of MRI images. To ensure the biocompatibility of these molecules we will investigate implementation of a biologically safe gold coating around the IONP. We will present what is observed in the characterization of these IONPs.

ACKNOWLEDGEMENTS:

Table of Contents

Table of Figures:

Table of Tables and Equations:

Chapter 1: Introduction

Magnetic resonance imaging (MRI) is a commonly used diagnostic scan that is noninvasive and allows for simpler detection and more assured diagnosis of many health complications. Early detection is crucial in many health complications including cancer which is the second leading cause of death following heart disease. Occurrence of cancer is quite common, 1:2 in men and 1:3 in women [1]. The increase in technology of treatment and the ability to diagnose cancer in its earlier stages have allowed survival rates to increase to nearly 70% in 2009 [1]. Early detection of cancer is beneficial for patients because it allows the improved treatments to be used to rid the patient of the abnormal cells.

The most common technique of detection is through the utilization of MRI scans where a technician is able to visually see the abnormal growth of the cells within the patient. MRI scans are safe for all patients that do not possess a foreign metal object within their body (pacemaker, implant, piercing, or bullet/fragments). MRI scans also have the ability to detect areas of damage in the brain and spinal cord that would normally be missed using other methods such as Computerized Tomography (CT/CAT scans) [2]. This is due to the fact that MRIs image soft tissue whereas CT scans image dense tissues such as bones. MRIs have been found superior to CT scans as a diagnostic device for the increase in accuracy and the fact that there is no radiation exposure [2]. An MRI scan without the use of contrast agents results in the image needed for diagnosis but tends to be blurry and decreases the assurance of a correct diagnosis. The addition of contrast agents, primarily gadolinium, greatly increases the clarity of MRI results and aids in increasing the accuracy of correct diagnosis.

Gadolinium-Based Contrast Agents (GBCAs) are a branch of drugs used in diagnostic imaging to increase the clarity of MRI scans. The GBCAs are administered intravenously soon before the scan takes place. Gadolinium has been used as a contrast agent for numerous years beginning with the first FDA approved GBCA Magnevist® in 1988 [3]. As of December 23, 2010 there were seven GBCAs approved by the Food and Drug Administration (FDA); Ablavar® (2008), Eovist® (2008), Magnevist® (1988), Multihance® (2004), Omniscan™ (1993), Optimark™ (1999), and Prohance® (1992) [3]. A relationship between GBCAs and Nephrogenic Systemic Fibrosis, an incurable life-threatening disease, was first introduced in May of 2006 [3]. This potential side effect of GBCAs is more than enough reason to find a different solution that does the same job with less risk to the patient. Therefore it is proposed that a biologically safe alternative of gold coated iron oxide nanoparticles can accomplish a similar degree of contrast improvement with a lesser risk of complications for the patient. There are several procedures for the synthesis of gold coated iron oxide nanoparticles. The following work outlines the steps taken to progress towards our goal of creating gold coated iron oxide nanoparticles such that we could then implement our own novel surface functionalization methods.

Chapter 2: Background and Theories

2.1: Magnetic Resonance Imaging (MRI)

Magnetic resonance imaging makes use of Nuclear Magnetic Resonance, specifically the sensitivity, to their immediate surroundings, of nuclei with non-zero nuclear spin. The hydrogen atom, for example, has a single proton and a nuclear spin of ½ [4]. The resonance frequency of the nuclear precession of the proton is extremely sensitive to the electron distribution of the surroundings; making it an effective probe of its environment. Other nuclei found in biological systems that can also give rise to locally influenced changes in magnetic resonance include: ^{13}C, ^{1}H, ^{31}P, ^{14}N etc. [4]. Due to the relative abundance of hydrogen in the body, found primarily in water molecules, proton based MRI (NMR) is by far the dominant method [5]. In fact, the body consists of about 70% water, which is distributed throughout nearly the entire body [5, 6]. A radio wave is applied in short pulses that disrupt the orientation of the magnetic moment, perpendicular to the applied magnetic field. As the magnetic moment becomes reestablished, time-dependent voltage shifts in the transverse plane are recorded [7]. The local shifts in proton resonance frequency are processed by a computer and arranged into a highly detailed black and white image that can show the small abnormalities. The computer arranges these images in a way that represents the patient by narrow slices that are placed together like slices of bread to make a loaf [6]. These slices can also be thought to be more like a rectangle with differential thickness and then integrated along the patient. Each slice is about a quarter of an inch thick and can be viewed from the bottom, front, and side views [7].

2.2: Relaxation/Relaxivity

Relaxivity is a characteristic associated with contrast agents used in MRI scans to increase the clarity and differentiation within the resulting images. The ability of a contrast agent to increase the rate of relaxation of the surrounding hydrogen spins per concentration of agent is called relaxivity [8, 9]. Relaxation rate is the amount of time required for the atom disrupted by a radio wave at the Larmor frequency to recover and reestablish its prior orientation in the magnetic field [10]. The reestablishment of the prior orientation results in two time measurements. The first being T1 time, also known as spin-lattice or longitudinal relaxation time, which is the time required for the net magnetic vector of the hydrogen atoms to realign with the direction of

Figure 1: Depiction of the T1 and T2 Relaxation Time Mechanisms [41]

the applied magnetic field [11]. The second is T2 time, also known as spin-spin or transverse relaxation time, which is the time required for the net magnetic vector of the hydrogen atoms to leave the plane perpendicular to the applied magnetic field [11]. These values are depicted in Figure 1. Different tissues in the body have specific relaxation times, due to relative water content, that are differentiated from each other within the results [8]. With increase in the relaxation rates of the hydrogen atoms, the differentiation between tissues is more easily achieved. This is why contrast agents are useful in MRI scans, because they allow for more definite differentiation of the tissues within the body and therefore can more readily detect abnormalities.

2.3: Gadolinium (Gd^{3+})

Gadolinium is the most commonly used element in contrast agents for MRI enhancement. It is a rare earth metal that is a part of the lanthanide series on the periodic table. The uniqueness of gadolinium lies in its unusual magnetic properties in its +3 oxidation state. In this trivalent state gadolinium becomes strongly paramagnetic and is utilized as a contrast agent in magnetic resonance imaging [12]. Paramagnetism is a property of a material such that it is not a permanent magnet but is attracted to external magnetic fields. Gadolinium (III) has 7 unpaired electrons that greatly increase the relaxation rate of water which in turn improves the clarity of MRI results in the area that the agent is administered [8]. It has been found that the use of these particular contrast agents have significantly decreased the T1 relaxation time which increases the clarity of areas observed such as plasma, liver, and kidney [13]. Gadolinium on its own is very toxic to the human body. In a gadolinium salt compound of gadolinium and chloride such as $GdCl_3$, acute toxicity is still a health concern [13]. Therefore, chelation with various ligands has been researched to reduce the toxicity of gadolinium within the body while maintaining the ideal magnetic properties as a contrast agent. The only concern with the method of chelation is the possibility that under certain internal environments, gadolinium could still be released within the body causing toxic effects on the individual [14]. The release of gadolinium is mainly a concern in the kidneys for it can be retained within them due to various causes of decreased nephrogenic function.

2.4: Gadolinium and Nephrogenic Systemic Fibrosis

Nephrogenic Systemic Fibrosis (NSF) is a disease attributed to the combination of decreased kidney function and infusion of GBCAs [3, 15]. It is a relatively uncommon

side effect of GBCAs when compared to the reported rush of heat throughout the body after being administered the drug. The seriousness of this rare side effect is what makes it so important. NSF is diagnosed in patients with chronic kidney failure and acute renal failure. 12% of patients with stage 5 chronic kidney diseases have been diagnosed with NSF after a single gadolinium exposure [15]. A patient diagnosed with this disease may develop thicker skin along with thickening and scarring of connective tissue. There are some cases of NSF where the disease progresses with such a rapid rate that the patient will experience joint contractures. These contractures can prevent movement at the affected joint, sometimes resulting in being bound to a wheelchair. The disease usually begins in the lower extremities and spreads from there over time and can lead to death; mortality approaches about 31% of patients [16]. Currently there is no treatment for NSF; there have been some cases of improvement of symptoms after a kidney transplantation that allowed renal function to be regained [15].

2.5: Why Iron Oxide Nanoparticles

Generally, atoms and molecules with higher electron spin will have a more significant influence on the local MRI probe nuclei (^{1}H) [4]. To a good approximation, the number of unpaired electrons in a material system can be used to estimate its potential as a contrast agent. As previously mentioned, gadolinium (Gd^{3+}) contains 7 unpaired electrons in its valence shell. Iron (Fe^{3+}) in iron oxide, Fe_3O_4, only has 5 valence electrons which would suggest that the magnetic properties of the iron nanoparticles would be less effective than gadolinium for use as a contrast agent. The 5 unpaired electrons of iron in Fe_3O_4 is a high estimate since there is the presence of Fe^{2+} as well with 4 unpaired electrons. Below 100nm in diameter, iron oxide nanoparticles are

superparamagnetic [17]. There are also differences in the use contrast improvement; gadolinium excels in increasing the quality of T1 weighted images where these iron particles assist in T2 weighted image quality enhancement [18]. The potential in iron oxide particles are due to their non-toxic contrast enhancing capabilities. There are numerous reasons that point to iron oxide nanoparticles, primarily Fe_3O_4, as a suitable replacement for gadolinium chelates. The biggest reason is the lack of toxicity to the human body in comparison to the chelated gadolinium ions [18].

2.6: Current Methods of Iron Oxide Nanoparticle Synthesis

There are several methods developed to synthesize iron oxide, Fe_3O_4, nanoparticles. These methods can be broken into two major groups depending on the mechanism used within the synthesis. Thermal decomposition and co-precipitation are the two most common methods described when considering iron nanoparticle synthesis [19]. Within these two categories there is even more diversity depending on chemicals used and desired size/quality of product [20].

Co-precipitation methods utilize stoichiometric mixtures of ferrous (Fe^{2+}) and ferric (Fe^{3+}) salts usually with the incorporation of ammonium compounds [21]. It is relatively easy to create large quantities of particles from this method. One of the benefits of this method is that the particles are synthesized within an aqueous solution, allowing the product to be directly precipitated into water [19, 21]. On the other hand one of the downsides to this process is the large and inconsistent size distribution of the particles which is important to consider when biological applications are possible [19]. Thermal decomposition is an alternative approach to the synthesis of iron oxide nanoparticles that utilizes higher temperatures paired with a variety of different organic compounds [22].

Downsides to this method include only the fact that the resulting particles are coated with a hydrophobic surfactant that impedes its dispersion in aqueous solutions [19]. Advantages for this method are its ability to produce narrow size distributions with tunable particle diameters while maintaining a high yield of particles.

The initial decision between which method to investigate first was based on the fact that the thermal decomposition method showed a better control over the size distribution, which we felt was more important in consideration of biological applications [19]. The advantage of co-precipitation was that the end result would already be in the desired aqueous solution which was enticing, but the concerns of various sizes initially clouded our judgement. One article compares both methods and notes that the size distribution of the co-precipitated product had a size distribution from about 20-90nm, average of 30nm, in diameter where the thermal decomposition data showed a size distribution of 6-35nm, average of 14nm, in diameter [19]. With this data it was clear to see that if any control over the size was desired, thermal decomposition was the method to experiment with and utilization of various extraction methods would be investigated.

Chapter 3: Methods of Characterization

3.1: Theory of Ultraviolet-Visible Light Spectroscopy

Ultraviolet-Visible Light Spectroscopy, more commonly referred to as UV-Vis

spectrometry, is a technique used in analytical chemistry applications to characterize

$$Absorbance = -log_{10}\left(\frac{I}{I_0}\right) = Concentration \cdot \varepsilon \cdot l$$

Equation 1: Beer Lambert Law

materials. Light sources are used, either one or two, to emit light over the ultraviolet and

visible light spectra (200-800nm) [23]. The maximum intensity of light is the incident

light (I_0), which passes through the sample and is absorbed within the sample. The

intensity of the transmitted light (I) is used in the Beer-Lambert Law, Equation 1, to solve

for concentration of analyte within the sample. This relationship requires the knowledge

of the path length (ℓ), which is the distance traveled by the light through the cuvette,

commonly 1cm. The molar extinction coefficient (ε) of the analyte, which is a

measurement of how strongly the analyte absorbs light at the specific wavelength, is also

required. UV-Vis Spectroscopy is also useful in characterizing solutions of transition

metals and organic compounds [23]. Solutions of transition metals tend to have distinct

color characteristics and therefore corresponding peaks. Organic compounds are

differentiated by their bond structures and functional groups when analyzing the peaks in

a given spectrum [23].

3.2: Theory of Fourier Transform Infrared Spectrometry

Fourier Transform Infrared (FTIR) spectrometry is a complex method of

spectroscopy with the ability to identify materials and determine the quality of a sample.

This method identifies materials by the "fingerprints" of molecules, as each FTIR

spectrum is unique to the measured molecule [24]. What separates FTIR from other methods of spectrometry is the inclusion of an interferometer within its working parts. The interferometer consists of a beam splitter and two mirrors [25]. The incoming infrared beam from a laser source passes through the beam splitter and changes into two separate identical beams. One beam reflects off a fixed mirror where the second beam reflects off a mirror that moves a few millimeters over time. The reflected beams rejoin at the beam splitter. The moving mirror allows continuous change of the reflecting beam such that it interferes with the other. This allows for the unique property in which the resulting beam contains every infrared frequency originating from the source [25]. The resulting beam then passes through the sample and is absorbed at different frequencies that correlate to the bonds within the molecule and the bonds' bending and stretching frequencies [24]. Since the plot involves measurements of absorbance at each frequency it is difficult to directly decode. Therefore a Fourier transform is performed manipulating the data such that it can easily be read and compared to other spectra for determination [25].

3.3: Theory of X-Ray Photoelectron Spectroscopy

X-Ray Photoelectron Spectroscopy (XPS) utilizes an x-ray to excite electrons within a sample located in an ultrahigh vacuum [26]. If the binding energy of the electrons is less than the energy of the x-ray, then the electrons will leave their respective orbit of the sample atom. If the electron is too deep within the sample, about 100 angstroms, then the electron will be reabsorbed within the sample and will not leave the sample [27]. Electrons closer to the surface (less than 100 angstroms) are not reabsorbed and are emitted from the sample [27]. Those that leave the sample travel between two

parallel plates that have opposite charges creating an orbit for the electron to pass through to a detector. The opposite charges allow selectivity over the electron as it travels depending on its energy. It is by varying the potential across these plates that a plot is created from the XPS readings [27]. Each time an electron hits the detector the energy, as it corresponds to the potential of the plates and the electrons binding energy, is recorded by a peak. Since each molecule's electrons have different energy levels, it is possible to determine the composition of molecules by this method [26, 27].

3.4: Theory of Dynamic Light Scattering

Dynamic light scattering (DLS) uses a light source that emits through a solution containing particles and measures the amount of light reflected from the particles. The software paired with the device allows for complex calculations to relate the amount of light to the size and distribution of particles in the solution [28]. Particles within a liquid solvent undergo Brownian motion, which is an unpredictable traveling pattern of the particle due to contact with other particles and surrounding solution [28]. In dynamic

$$D = \frac{\Gamma}{\left(\frac{4 \cdot \pi \cdot n_o}{\lambda_o} \cdot \sin\left(\frac{\theta}{2}\right)\right)^2}$$

Equation 2: Correlation Relationship

light scattering Brownian motion is utilized in the calculations. As the particles move within the solution there is a slight time difference, and therefore light intensity difference, which is measured by the device [29]. Through analysis of multiple correlation functions, the decay rate (Γ), the angle of scattered light (θ), the vacuum wavelength of incident light (λ_o), and the refractive index of solvent (n_o), the software has the capability to calculate a diffusion coefficient (D), shown in Equation 2 [29].

The last calculation necessary follows the Stokes-Einstein relationship, Equation 3, where the calculated diffusion coefficient is used with solvent dynamic viscosity (η), temperature (T), and the Boltzmann constant (k) [29]. This last calculation gives the hydrodynamic radius (r_h) of the particles that were measured by the device via their scattered light.

$$r_h = \frac{k \cdot T}{6 \cdot \pi \cdot \eta \cdot D}$$

<div align="center">Equation 3: Stokes-Einstein Relationship</div>

The results from the DLS allow for graphical readings showing the size of the particles based on the intensity reading, the size by volume of solution, and the size by number of particles. Various calculations showing quality of the solutions dispersity are also calculated to fully analyze the sample.

3.5: Theory of Transmission Electron Microscopy

Transmission Electron Microscopy (TEM) is a technique that utilizes electrons as a "light source" to create extremely high resolution images of samples [30]. TEMs use a tungsten filament to send electrons through a vacuum column within the microscope to the sample [31]. Common light microscopes use various focusing lenses to direct light from sample to observation lenses. The TEM uses electromagnetic lenses to focus the electrons into a thin beam, which is then passed through the sample [31]. As the electrons pass through the sample they are affected by the varying densities of the sample. In areas of the sample that have a lesser density, more electrons pass through to the phosphor film leaving a brighter area of the image. Darker regions of the images are due to denser areas of the sample where fewer electrons pass through. This allows the resulting images to have the resolution of about 0.2nm [31].

Chapter 4: Experimental Procedures

4.1: Thermal Decomposition Method

Using the thermal decomposition method has been shown in previous works to produce a narrow distribution of particle sizes. A mechanism for how this method forms the Fe_3O_4 nanoparticles is presently unclear. Figure 2 shows a depiction of the reaction and how the particles are synthesized from the reactants. Evidence suggests that the formation involves reduction of the Fe (III) salt into a Fe (II) intermediate [22]. This
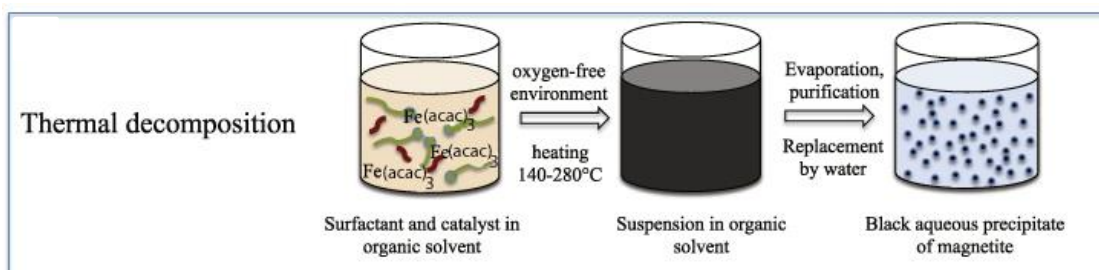
Figure 2: Depiction of Thermal Decomposition Method [32]

intermediate is then decomposed at the high temperatures reached. The Fe (III) salt used is Iron (III) acetylacetonate that is reduced by 1,2-Hexadecanediol. The addition of oleylamine and oleic acid are used to cap and coat the particles leading to consistent sizing and the hydrophobicity of the particle surface. The oleic acid has a carboxylic acid group that directly binds to the iron oxide surface, as a carboxylate, stabilizing it within organic solvents [32]. Phenyl ether is used as the initial organic solvent for its boiling point is higher than necessary for the 4 nm synthesis. Larger particles procedures require higher temps and therefore benzyl ether is necessary.

4.1.1: Experimental Setup

Setting up the experiment, shown in Figure 3, consists of a three-neck round-bottom flask with a condensing column attached to the middle neck. A straight

Condensing Column

Thermocouple

Water out

Nitrogen

Input of Chemicals

Water in

Stirring Bar

Sand Bath

Hot/Stirring Plate
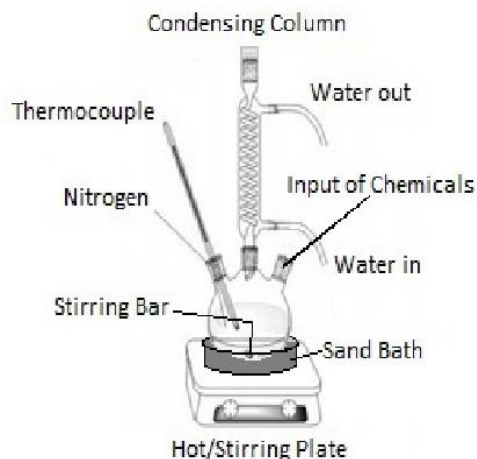
Figure 3: Schematic of Experimental Setup [16]

condensing column is preferred over a spiral column for phenyl ether crystalizes within the spirals leading to pressure related complications. The condensing column has water attached to enter in the bottom barb and exit out of the upper barb for cocurrent flow. The flask is in a sand bath which is paced on top of the hot plate. A properly sized stirring bar needs to be inserted into the flask for physical agitation of the reaction. A hose is fixed to a needle that is punctured through a rubber septum to provide nitrogen into the system as well as to seal the leftmost neck. The same is done with the thermocouple to closely monitor the temperature of the reaction. Alternatively, a thermometer can be placed in the sand bath at the approximate position of the liquid level within the flask. The rightmost neck is left open until the chemicals are inserted and then sealed with a rubber septum. This forces all nitrogen and vapors of the reaction to exit the condensing column where the vapors will reflux and return as liquid back into the reaction. When joining the glassware together it is beneficial to apply a small amount of glycerol to each part of contact. This is because of the crystallization of phenyl ether during the refluxing period and the glycerol helps to prevent possible damage to glassware.

4.1.2: Iron Oxide Nanoparticle Synthesis, 4nm

The following procedure has been adapted from a procedure in *Monodisperse MFe$_2$O$_4$ (M=Fe, Co, Mn) Nanoparticles* (4 nm) [22]. The synthesis of the iron oxide nanoparticles involved a variety of chemicals that are outlined below in Table 1. The

amount given in literature was in moles and was converted to mass/volume and then

adjusted for the amount used in our "quarter-batch" trials.

Table 1: Chemicals Involved in Iron Oxide Nanoparticle Synthesis

Chemical	Material Type	Amount [mmol]	Converted amount	Amount used
Iron (III) Acetylacetonate	Solid, Powder	2	0.706 grams	0.178 grams
1,2-Hexadecanediol	Solid, Powder	10	2.584 grams	0.646 grams
Oleic Acid	Liquid	6	1.904 mL	500 µL
Oleylamine	Liquid	6	1.974 mL	500 µL
Phenyl Ether	Liquid	N/A	20 mL	5 mL

The procedure began with flooding the experimental setup with a blanket of

Nitrogen to create an inert environment. The chemicals are weighed and prepared while

the system is flushed with nitrogen. A mask must be worn when weighing out the

powdered 1,2-Hexadecanediol for it is a potential hazard to the respiratory system. After

the system has been flushed with nitrogen for about 5 minutes, the chemicals are added to

the three-neck round-bottom flask. It was observed during multiple iterations of this

procedure that it is more efficient to add all of the solid "dry" ingredients first. This is so

residual amounts of the powders that stick to the neck of the flask may be washed into the

reaction using the liquid chemicals. This process ensures that all of the amounts of

chemicals will be utilized in the reaction.

When all of the chemicals are added the hot plate is turned on and the temperature

is increased to 200˚C. The stirring was set at 250 rpm; this was determined by

observation of severe bouncing of the stir bar at higher settings. Once the reaction had

reached 200˚C the temperature of the hotplate was decreased to maintain the reaction

temperature at 200˚C for 30 minutes. After this step the hot plate temperature is increased

again to reach a reaction temperature of 265˚C. Once this temperature is reached it is held

there to reflux for 30 minutes. After the second reflux period it is dire to place a rubber

septum in the top of the condensing column. This allows trapping of the reaction under inert gas preventing oxidation. Simultaneously, the nitrogen source needs to be turned off so the pressure of the system does not build to the point where the stoppers blow out of the necks. With the system disconnected from both the nitrogen and water lines, it is then raised out of the sand bath and left to cool to room temperature while under its inert environment.

4.1.3: Application of Centrifugation

Centrifugation is a common practice in most lab settings when the separation of solids from within a liquid suspension is necessary. The theory behind centrifugation stems from that of sedimentation, which is an act of gravity. Sedimentation occurs when particulates are removed out of a solution to the bottom of the container when the force of gravity overcomes the buoyancy and viscous forces of the particles. Sedimentation occurs over a relatively long period of time. Centrifugation imposes an additional force to that of gravity at a larger magnitude to speed up the precipitation of particulates. This extra force is the relative centrifugal force (RCF), Equation 4, which consists of angular velocity (speed of spinning sample in a circle) and the radius of the circular motion (radius of the rotor).

$$RCF = 1.1118 \times 10^{-5} \cdot Radius(cm) \cdot Speed(rpm)^2$$

Equation 4: Centrifugal Force Relationship

The centrifuge holds the sample tubes at a fixed angle in a rotor and can spin the rotor at speeds surpassing 150,000 rpm, creating over 1 million times the force of gravity. Rotors come in different sizes where larger radii cause larger forces at the same speed, and similarly, higher speeds create larger forces at the same radius.

4.1.4: Iron Oxide Nanoparticle Centrifuge Process

The following centrifuge protocol was adapted from *Monodisperse MFe$_2$O$_4$ (M=Fe, Co, Mn) Nanoparticles* (4 nm) [22].

The centrifuge procedure consists of 3 stages of centrifuging to separate the synthesized iron oxide nanoparticles from the chemical solution. The first stage of the centrifuge process consists of adding 10mL of Ethanol to the iron solution and then transferring the chemical solution from the three-neck round-bottom flask into a 35mL centrifuge tube. An additional wash step of the flask may be necessary if there is visible product remaining in the flask after transfer. The wash step would consist of the initial solvent Phenyl Ether and additional Ethanol in amounts of 1mL and about 5mL respectively. The centrifuge tube is balanced against a second tube filled with water, and then spun for 10 minutes at 6,000 rpm. In this step the particles are dissociating from the ethanol and phenyl ether. When the centrifuge has stopped, the tubes will have a pellet in the bottom of them, see Figure 4. This contains the particles and is kept for the next spin.

Figure 4: Iron Nanoparticles Separated by Ethanol via Centrifugation

The second stage of the centrifuging process starts with decanting the fluid out of the tube from the first spin, keeping the pellet intact. Next is the addition of the following to the tube containing the pellet: 5mL of Hexane, 25μL of Oleic acid, and 25μL of Oleylamine. The tube is then mixed in the vortexer to disperse the pellet in the liquid; this is done until the pellet is not visible. The tube is once again balanced with respect to the tube of water and spun for 10 minutes at 6,000 rpm. This step in the process can be extended to a 30 minute

spin to ensure the removal of unwanted particulate. The end result of this spin also contains a pellet but this time the top layer is kept and the pellet is disposed of. The top layer consists of the wanted particles suspended in hexane where larger aggregates that are too large for suspension in hexane create the pellet that is disposed of.

The final stage of the centrifuging process begins with the liquid layer from the previous stage. To the liquid layer, 10mL of Ethanol is added and mixed once more. The tube is then balanced and spun once more for 10 minutes at 6,000 rpm. Once the spin has ended and the tube has had a chance to allow settling and separation. A clear separation of layers will become visible. The top layer consists primarily of Ethanol and needs to be decanted from the bottom layer which once again is hexane with suspended particles. Once the bottom layer has been obtained, it is transferred from the centrifuge tube to a glass vial. Any extra space in the glass is filled with hexane and left for further testing, thus ending the synthesis procedure of the iron oxide nanoparticles.

4.1.5: Coating of Iron Oxide Nanoparticles with Gold

The following procedure has been adapted from a procedure in *Monodispersed Core-Shell Fe3O4@Au Nanoparticles* [33]. The addition of a gold shell to iron oxide nanoparticles involves the chemicals outlined below in Table 2. Similar to the previous procedure table the amount given in moles was converted to mass/volume and then quartered for the amount used in our trials.

Table 2: Chemicals Involved in Addition of Gold Shell to Iron Oxide Nanoparticles

Chemical	Material Type	Amount [mmol]	Converted Amount	Amount Used
Gold (III) Acetate	Solid, Powder	2.2	0.823 grams	0.208 grams
1,2-Hexadecanediol	Solid, Powder	12	3.101 grams	0.775 grams
Oleic Acid	Liquid	≈1.5	0.476 mL	125 μL
Oleylamine	Liquid	≈6	1.974 mL	750 μL
Phenyl Ether	Liquid	N/A	30 mL	7.5 mL
Synthesized Iron Particles	Liquid	≈0.33	≈10 mL	2.5 mL

The experimental setup for the addition of the gold shell to the iron oxide nanoparticles is the same for that of synthesizing the iron oxide nanoparticles (see Figure 3). It is important to note that the iron oxide particle solution added here is directly from the previous reaction. It has not been centrifuged and the ethanol has not been added. The first step in this procedure is to flood the system with nitrogen to create an inert environment. Once the nitrogen has flushed the system for about 5 minutes, the chemicals can be added. Solid ingredients should be added first with the liquid ingredients following, see Table 2. This order of ingredients is important so the liquid ingredients can wash down any residual amounts of the solid ingredients on the glassware and maintain a 7:1 gold to iron molar ratio. Once all of the ingredients have been added, the temperature of the reaction is increased to 180-190°C at a rate of 10°C per minute. Once at 180-190°C, the temperature must be held at this point for 90 minutes. After the heating process, the reaction is left to cool to room temperature. Once cooled, 25mL of Ethanol is added to the reaction before the centrifuge process.

4.1.6: Gold Coated Iron Oxide Centrifuge Process

The following centrifuge protocol has been adapted from a procedure in *Monodispersed Core-Shell Fe3O4@Au Nanoparticles* [33].

The solution of nanoparticles is transferred to a centrifuge tube and balanced against another tube of water and placed into the centrifuge. The tubes are spun for 20 minutes at 7,000 rpm. At the end of the spin, a pellet should
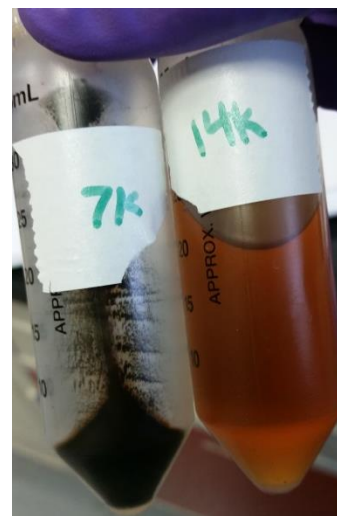
Figure 5: Gold Coated Iron Oxide Nanoparticle Pellet (Left) and Resulting Top Layer (Right)

be observed as well as the top liquid layer remaining a dark purple color. Our first spin resulted in a pellet, but the top layer was a golden liquid similar to an ethanol top layer with iron remnants, see Figure 5. The pellet is washed with ethanol and redispersed in hexane along with oleylamine and oleic acid with the latter two at concentrations of 75 mM.

The top layer was kept from the first spin and spun once again, after being balanced with a tube of water, for 20 minutes at 14,000 rpm. This should again form a pellet and a golden colored top liquid layer containing remnant iron particles. In our case we spun a second time to remove all possible gold nanoparticles. The result was the same liquid, without a pellet, indicating all particles in the solution were removed in the prior spin.

4.1.7: Iron Oxide Nanoparticle Phase Transfer

Figure 6: Iron Oxide Nanoparticles Top Layer, PEG Solution Bottom Layer

The final product of the thermal decomposition method results in the iron oxide nanoparticles dispersed in an organic solvent, in our case hexane. To proceed further with characterization and potential biological applications, the nanoparticles would have to be removed from the organic phase and dispersed in water. Several methods of this phase transfer have been investigated using a variety of molecules. The methods we found as most promising for extraction of the particles and attempted are as follows: Polyethylene glycol (PEG), amino hydroxyl PEG, α-cyclodextrin [34], and tetramethylammonium 11-aminoundecanoate [22, 35].

The use of PEG was motivated by its success in diverse extraction situations. PEG was mixed in water at a 1% (w/v) where 3mL of the solution was placed in a vial with 1mL of the particle solution, see section 4.1.4, and was placed on the shaker table for several days with no results shown, see Figure 6. The next attempt involved using a PEG molecule with an amine group on one end of the polymer chain and a hydroxyl group on the opposite end. There have been observations that the amine groups coordinate with the iron surface [22]. The amino hydroxyl PEG was used in the same manner as the previous PEG and signs of the phase transfer were again nonexistent.

The next method we attempted utilized α-cyclodextrin at a concentration of 5 mM and used with equal volumes of sample [34]. Recent experiments of this method allow it to stir for 20 hours such that the α-cyclodextrin binds to the oleic acid molecules changing the hydrophobic behavior of the surface to a hydrophilic one [34]. The color is noticed to leave the hexane top layer and diffuse into the water bottom layer transferring all of the particles into water. We allowed several days for our two phases to transfer on a shaker table providing a constant disturbance of the bi-liquid interface. No color change had occurred resulting in no transfer of the particles out of the hexane solvent.

Oleic acids being the reason that the particles are not dispersible in water lead to the intent of removing the oleic acid from the particles such that we could readily disperse them in water. It has been shown that tetramethylammonium 11-aminoundecanoate removes the oleic acid layer from the Fe_3O_4 nanoparticle surface [22, 35]. We used a concentration of 20 mg
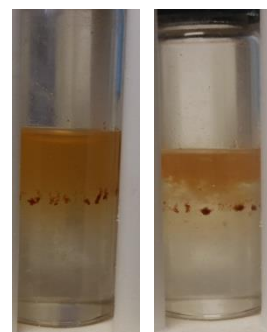
Figure 7: Attempted Phase Transfer of Iron Nanoparticles by Removing Oleic Acid.

of tetramethylammonium 11-aminoundecanoate in 2 mL of dichloromethane [22] and placed 1mL of our iron particle solution on top and again placed it on the shaker table for several days, Figure 7. In a separate tube we used equal volumes of dichloromethane solution and iron nanoparticle solution and shook it more vigorously and there was no color change but a pellet had started to form in the bottom of the vial. The pellet was not black and therefore led us to believe it was oleic acid and the particles were being stripped of it. We centrifuged the mixture at stages

Figure 8: Resulting Pellet from Centrifugation of Phase Transfer Attempt

(started at 1krpm, increased by 1krpm each stage) in an attempt to salvage some of the "bare" particles and collect the oleic acid as a pellet, Figure 8. When presumably bare particles were left, we attempted to disperse them in water with a small amount of acetic acid. The particles would disperse in water but would not stay dispersed for a reasonable amount of time and would sediment relatively quickly out of solution.

4.1.8: Gold Coated Iron Oxide Phase Transfer

In an attempt to phase transfer the gold coated iron nanoparticles from the hexane solvent into water, similar to our attempt of removing iron nanoparticles from hexane in the previous section, we tried the following molecules: PEG and PEG-thiol. Knowing that the PEG was unsuccessful in the iron oxide particle procedures, we still made an attempt for the gold coated particles hoping for different results. We followed the same procedure as above in the iron extraction section. The concentrations of PEG used in water was 1% (w/v) where 3 mL of the solution was used in a vial with 1 mL of the

sample on top of that. The PEG used did not permit the transfer of the particles from the hexane layer to the water.

PEG-thiol was the next option for an attempt to extract the gold coated nanoparticles. The theory behind the use of this polymer was based on the fact that sulfur and gold form a covalent bond to each other in a nearly irreversible manner. The junction between gold and sulfur is robust and understanding these fine details is crucial for the control of ligand-exchange reactions [36]. The PEG-thiol was prepared in water at a 1% (w/v) concentration. 3 mL were used in a vial as 1 mL of our gold sample was added as well. Knowing that the oleic acid has coated the gold nanoparticles, it was believed that the PEG-thiol would be energetically favored and bind to the surface of the gold coating displacing the oleic acid. The sample was shaken for nearly a week on a shaker table and

Figure 9: Phase Transfer of Gold Coated Iron Nanoparticles Using PEG-Thiol

showed no evidence that a phase transfer had or was going to take place, see Figure 9. Possible reasons as to why these phase transfer methods did not work will be discussed in the results.

4.2: Co-Precipitation Method

The co-precipitation method utilizes two iron sources dissolved in water at room temperature, Figure 10. The two reactions that take place are the decompositions of both the Fe^{3+} source to FeOOH and the Fe^{2+} source to $Fe(OH)_2$ [37]. Following the individual decomposition is a solid state reaction between the two previous products. This results in the creation of Fe_3O_4 and 2 molecules of water [37]. The reaction is designed to utilize the necessary ratio of 2:1 of Fe^{3+} and Fe^{2+} as well as the concentration of OH in the

$$2Fe^{3+} + Fe^{2+} + 8OH^- = 2Fe(OH)_3Fe(OH)_2 \text{ (s)} \rightarrow Fe_3O_4 \text{ (s)} + 4H_2O$$
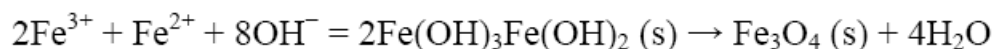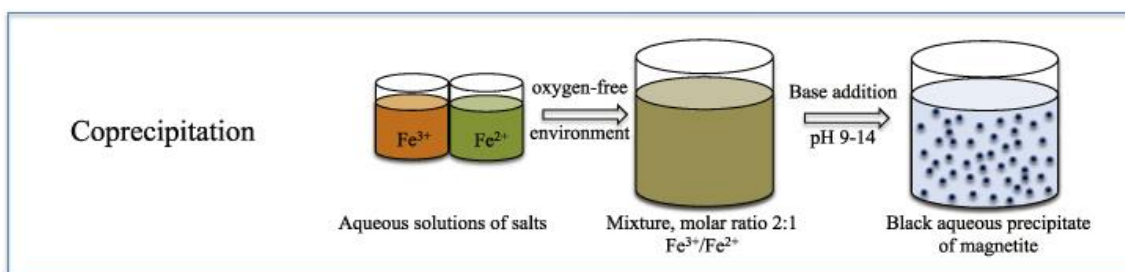
Figure 10: Depiction of Co-precipitation Method [32] and Reaction Mechanism [37]

reaction. To ensure the presence of OH, a basic pH level, strong bases are added for the

[OH] controls the growth and nucleation of the particles [37].

4.2.1: Experimental Setup

The experimental setup for the co-precipitation methods in comparison to the

thermal decomposition differs only in the bath used for heating, Section 4.1.1. An oil bath

is used in the co-precipitation method for the temperatures are low enough to use oil and

it provides more consistent heating than a sand bath. The condensing column and

nitrogen are still used to prevent rapid oxidation of the particles when in contact with the

air and to condense any water vapor from boiling off completely during the higher

temperature stage.

4.2.2: Iron Oxide Nanoparticle Synthesis

The following procedure has been adapted from a procedure in *Self-Assembly*

Mechanism of Spiky Magnetoplasmonic Supraparticles [21]. Amounts of chemicals used

Table 3: Chemicals Involved in Co-precipitation of Iron Oxide Nanoparticle Synthesis

Chemical	Amount
Iron(II) Chloride Tetrahydrate	1.622 grams
Iron(III) Chloride Hexahydrate	0.994 grams
Ammonium Hydroxide solution (~28%)	5 mL
Sodium Citrate	4.4 grams

in this process are outlined in Table 3.

The experiment starts with dissolving both the $FeCl_2 \cdot H_2O$ and $FeCl_3 \cdot H_2O$ in 40 mL of water while stirring. The speed of the stirring was set to 500 rpm, to assist in dissolving the iron compounds, and the speed was used throughout synthesis unless otherwise noted. Once the iron compounds have completely dissolved, 5 mL of the ammonia solution is quickly added to the reaction solution and the reaction is left to sit undisturbed for 10 minutes, stirring is turned off. After allowing the solution to sit, the sodium citrate is added, the temperature is raised to 90°C for 30 minutes, and continuous stirring is resumed. When the heating time is completed the reaction

Figure 11: Magnetic Separation of Iron Oxide Nanoparticles from Aqueous Solution

is cooled to room temperature in which a black precipitate forms in the bottom of the reaction vessel. The precipitate is washed several times with water by using a magnet to hold the precipitate, add water, and decant the top layer of liquid, Figure 11. After sufficient repetitions of the wash step, half of the precipitate was left to dry in an oven set to 40-45°C. The solution used to allow drying was taken after a sample was already removed for the next step, coating the iron nanoparticles with gold.

4.2.3: Coating of Iron Oxide Nanoparticles with Gold

The following procedure has been adapted from a procedure in *Self-Assembly Mechanism of Spiky Magnetoplasmonic Supraparticles* [21]. Chemicals and respective amounts used in this process are outlined in Table 4.

Table 4: Chemicals Involved in First Method of Adding Gold Shell to Iron Oxide Nanoparticles

Chemical	Amount
Hydrogen Tetrachloroaurate Trihydrate (0.5mM)	20 mL
Fe3O4 Nanoparticle Solution (0.136µM-NPs)	10 mL

The preparation of coating the previously synthesized iron oxide particles with gold begins with 20 mL of 0.5mM hydrogen tetrachloroaurate (III) trihydrate. This gold solution was brought to a boil and then the addition of 10 mL of the 0.136µM, concentration of Fe_3O_4 nanoparticles in water followed soon after. The concentration involves analysis of the Fe atoms within the unit cell of Fe_3O_4, in regards to initial chemicals added, as well as consideration of particle size in the resulting participate. We calculated this value and to achieve this concentration involved dispersing the product in the same amount of water as added initially, 40 mL, see Appendix I. The addition of the iron solution was completed as the reaction solution was under continuous stirring. At this point the solution undergoes a color change from a brownish color to more of a burgundy. The color change completes after about 10 minutes of heating and stirring. After the color change is completed the heat source is removed and the solution is allowed to cool to room temperature. The particles are once again separated via magnet and then washed multiple times with water.

A second method which varied slightly in this process was utilized in an attempt to ensure the appropriate amount of sodium citrate on the surface of the iron such that it would accept the gold coating. The following procedure was adapted from a procedure in *Application of citrate-stabilized gold-coated ferric oxide composite nanoparticle for biological separations* [38]. This literature synthesized Fe_2O_3 for the core where we are using Fe_3O_4; just the gold coating methods were adapted. Amounts of chemicals used in the adapted process are shown in Table 5.

Chemical	Amount
Hydrogen Tetrachloroaurate Trihydrate (0.5mM)	20 mL
Fe3O4 Nanoparticle Solution (0.136μM-NPs)	1 mL
Sodium Citrate	0.129 grams

This method started with the dilution of 1 mL of our iron solution in 50 mL of 0.01M sodium citrate. The diluted solution was stirred for 30 minutes to ensure that the citrate coated the surface of the iron particles. 20 mL of the stirred iron solution was brought to a boil and once it has boiled 20 mL of 0.5mM of the gold solution, same as previous method, is added immediately. This mixture is kept at the same temperature and stirred for 15 minutes. After the time has passed, the heat is removed and the stirring continues as it cools to room temperature. The solution is separated by magnet and washed multiple times with water.

Unfortunately, with both of these methods, we redispersed the product in water and took dilutions of the samples to compare them colorimetrically. The results of this basic comparison suggest that both methods of gold coating did not allow for the gold to be exchanged for the citrate ions on the surface of the iron cores. The colors that were to be expected were in the range of red to purple depending on the ratio of gold coating the surface to iron. As seen in Figure 12, the colors of the samples seem to be the same and brown. The only noticeable difference is that of the rightmost vial, it is slightly more transparent than the other two. This is most likely due to being a sample of the second method of gold coating where the iron is diluted in a citrate solution prior to boiling. The leftmost tube is diluted iron solution and the middle tube is the first gold coating method that uses a larger volume and higher concentration of iron when compared to the rightmost tube.
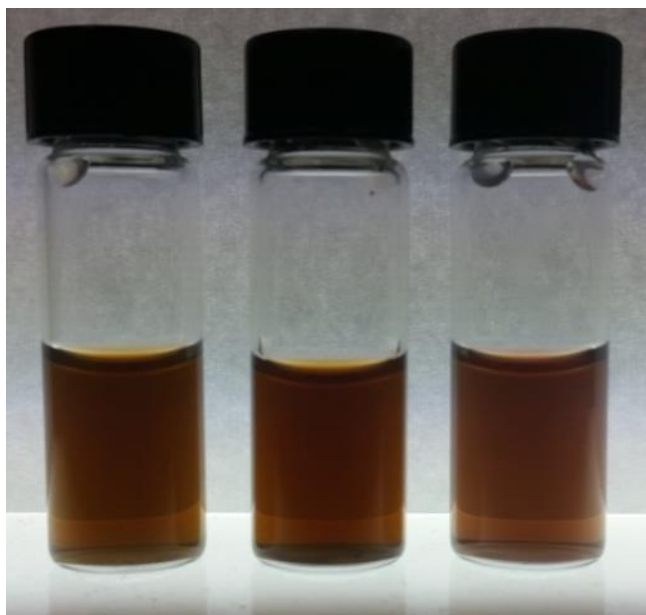
Figure 12: Dilutions of Co-Precipitation Products. From Left to Right: Iron Oxide Nanoparticles, First Gold Coating Method, and Second Gold Coating Method

Chapter 5: Results

5.1: Ultraviolet-Visible Light Spectroscopy Results

The following UV-visible light spectroscopy results were analyzed in the

wavelength window from about 400 nm to 900 nm. This was due to an abundance of

noisy absorbance data below 400 nm. For visual ease of comparison, the data for the

wavelengths below 400 nm were omitted. The measurements pertaining to the thermal

decomposition method were made in reusable quartz cuvettes due to the hexane solvent,

to prevent damage to the plastic cuvettes with in the measuring devices, while the co-

precipitation measurements were made in disposable plastic cuvettes for the solvent is

water.

5.1.1: Iron Oxide Nanoparticles-Thermal Decomposition Method

The UV-Vis spectrum below, Figure 13, shows the absorbance pattern of the iron

oxide nanoparticles synthesized using the thermal decomposition method. The process

used to obtain this spectrum involves a 1:11 dilution of the iron solution, from the

centrifugation process, into hexane. Then we completed a simple 1:1 dilution of the
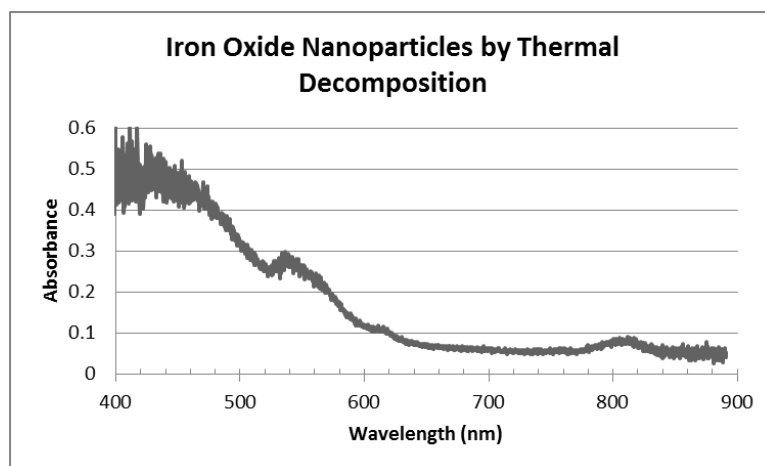
Figure 13: UV-Vis Spectrum of Iron Oxide Nanoparticles Synthesized via Thermal Decomposition

previous dilution, halving it.

5.1.2: Gold Coated Iron Oxide Nanoparticles-Thermal Decomposition Method

The spectrum for the gold coated iron oxide nanoparticles, Figure 14, was determined by analysis of a sample that was diluted twice using a 1:14 dilution of sample to hexane respectively. The iron oxide particles that were coated with gold are from the same product as described above by the spectra in Figure 13.
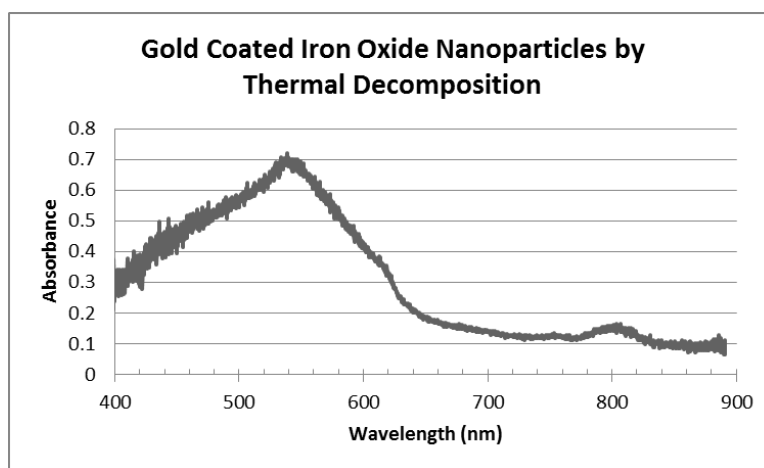
Figure 14: UV-Vis Spectrum of Gold Coated Iron Oxide Nanoparticles

5.1.3: Comparison of Spectra to Literature Values

Seen in Figure 15 are two spectra. The one on the left is data collected from the thermal decomposition method and have been singly described in the above sections. The spectra on the right is a literature value showing the absorbance patterns of Fe_3O_4 as well as gold coated iron oxide nanoparticles (denoted in the image as Fe oxide and Au-Fe oxide respectively). The various dashed lines for the gold coated particles correlate to a ratio of concentration of gold to iron in the reaction, seen in the index of the plot, the ratio ranges from 1-4.
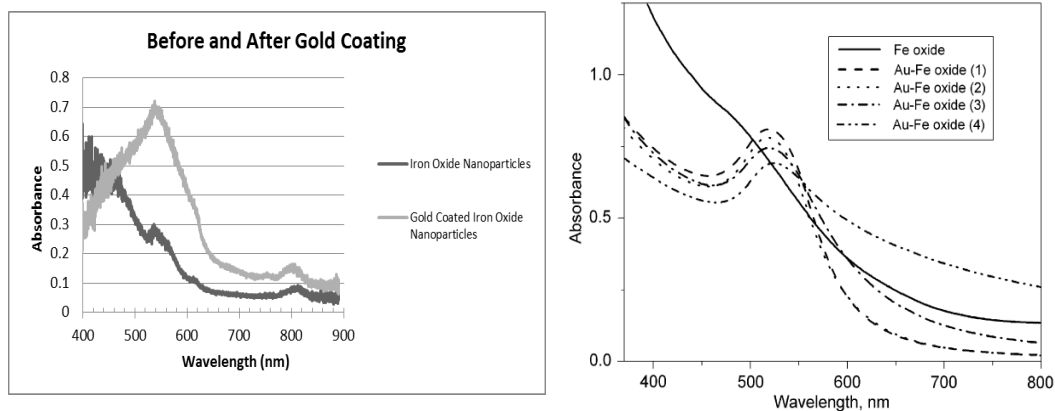
Figure 15: UV-Vis Spectra of Iron Oxide Nanoparticles and Gold Coated Iron Nanoparticles. Acquired Data on Left and Literature Values [38] on the Right

At first glance it seems obvious that the data acquired does not correlate to the literature values. A reason for this could easily be the concentration used in the UV-Vis analysis. It would seem that the concentration of the iron analyzed appears to be higher in the literature spectra for the absorbance values are higher, almost double of the acquired spectra. Following this observation we can see that the pattern of the spectra agree such that there is a steady increase to the upper left, starting at about 650 nm, with a slight rise in the values just to the left of the gold peak.

The spectra for the gold coated particles seem more compatible as they both show the peaks at an absorbance of about 0.7. The peak wavelengths also differ by a small amount where the literature value shows a peak at about 530 nm and the acquired spectrum on the left shows a peak of 540 nm. The small variation in the data we acquired can be attributed to either the noise in the acquired spectra due to the acquisition equipment, the difference in size distributions of the particles/thickness of gold coating, or to the assumed excess of oleic acid and oleylamine that most likely prevented the phase transfer processes attempted.

31

5.1.4: Iron Oxide Nanoparticles-Co-Precipitation Method

The below spectrum, Figure 15, shows the absorbance pattern of the iron oxide nanoparticles synthesized utilizing the co-precipitation method. The dilutions of this sample differed for it was a very dark concentrated black at the end of the synthesis process. The dilution of the sample followed as 50 μL in 2 mL of water (1:40) followed by an additional dilution of 1:4 using the previous dilution and water respectively. This allowed for the desired absorbance peak at around 0.5 seen below.
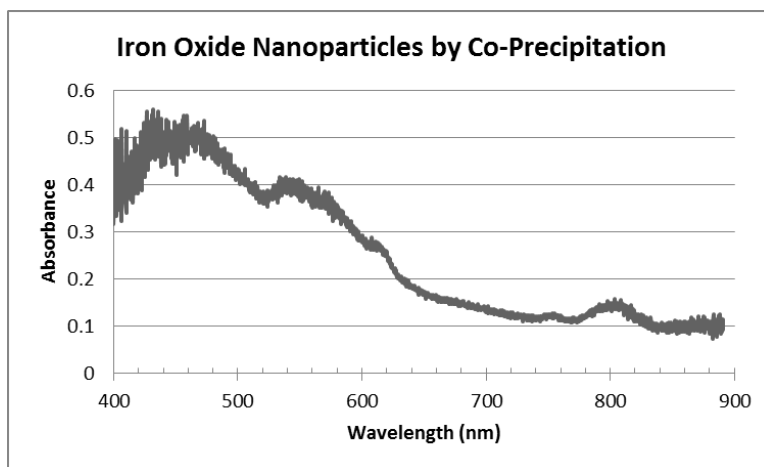
Figure 16: UV-Vis Spectrum of Iron Oxide Nanoparticles Synthesized via Co-Precipitation

5.1.5: Iron Oxide Nanoparticles-Comparison between Methods

Since there were two methods used to create the Fe_3O_4 iron oxide nanoparticles we felt a comparison between the two would be necessary to confirm that the products we were analyzing were the same. In Figure 17, the spectrum of iron oxide nanoparticles from both methods were superimposed upon each other. It is clear to see that the lines do not exactly run on top of each other and as aforementioned this can be attributed to the differing concentrations. The patterns of the lines, the peaks and valleys, match up perfectly suggesting that the particles synthesized from both methods are of the same composition.
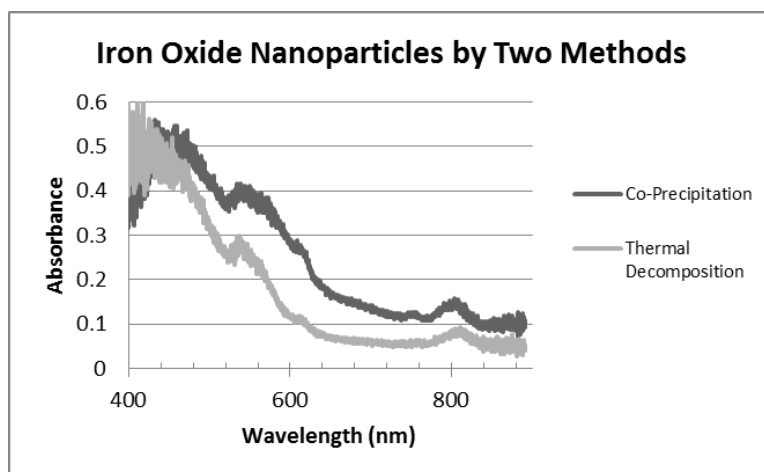
Figure 17: UV-Vis Spectrum of Iron Oxide Nanoparticles Synthesized by Two Methods: Thermal Decomposition and Co-Precipitation

5.2: Fourier Transform Infrared Spectroscopy Results

An accurate way to measure the quality of a sample is by utilizing a FTIR

spectrum. Figure 18 is the acquired spectrum of the iron oxide nanoparticles that were

synthesized via thermal decomposition. Due to the inability to phase transfer the particles

out of the hexane solvent we were led to believe there was an abundance of oleic acid

preventing the conversion of the iron oxide nanoparticles from a hydrophobic to the

necessary hydrophilic state. Figure 19 shows a FTIR spectrum of oleic acid coated

magnetite particles [39] in which a comparison is made between this reference and the

acquired spectrum. By looking at both spectrums you can see similarities right away

showing that the particle solutions in both cases are very similar in composition. A major

difference is the strong broad peak in the reference spectrum at 3417 cm^{-1} which is

characteristic of O-H stretches, commonly water, but is attributed to hydroxyl groups that

bind to the iron surface where the surfactants aren't present [39]. The acquired spectrum

is without that peak, suggesting an abundance of surfactant, oleylamine and oleic acid,

coating the particles' surface leaving no opportunity for hydroxyl group binding.

33
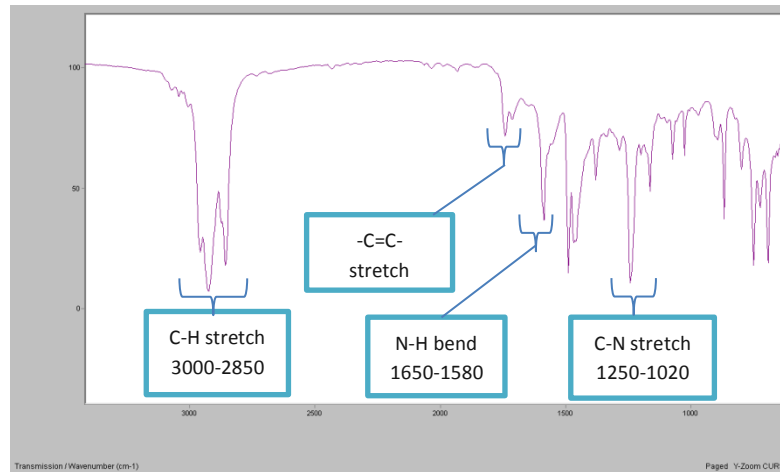
Figure 18: FTIR Spectra of Iron Oxide Nanoparticles synthesized via Thermal Decomposition. X-axis is in Wavenumber (cm^{-1}), Y-axis is % Transmittance

Other peaks of interest are those of the C-H stretch as it seems broader in the acquired spectrum where width can be attributed to more of that type of bond, present in both oleic acid and oleylamine. The peaks in the acquired data also confirm the presence of carbon double bonds present in both oleic acid and oleylamine. Two peaks attributed to N-H bends and C-N stretches are prominent in the above spectrum showing presence of oleylamine due to its terminal primary amine group.
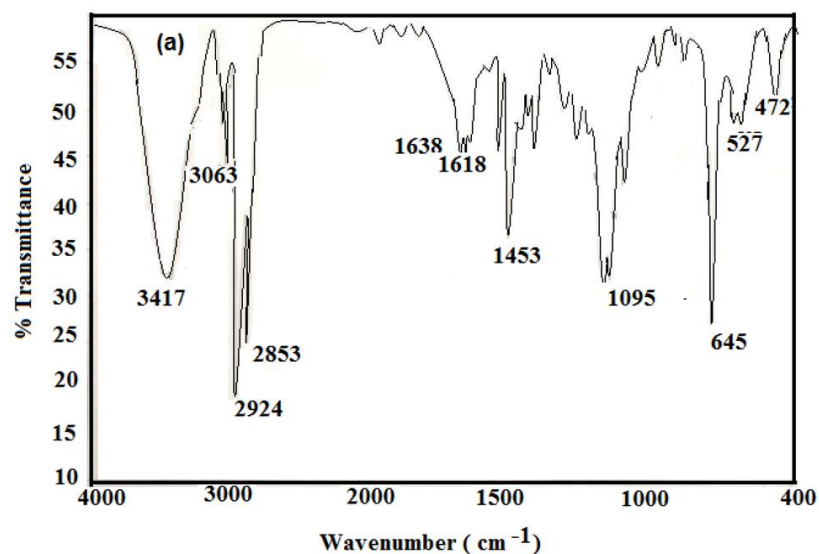
Figure 19: Literature Representation of Oleic Acid Coated Magnetite [39]

34

5.3: X-Ray Photoelectron Spectroscopy Results

To determine the composition of our particles we utilized X-Ray Photoelectron Spectroscopy (XPS) data seen in Figure 20. The leftmost spectrum is and enlarged view
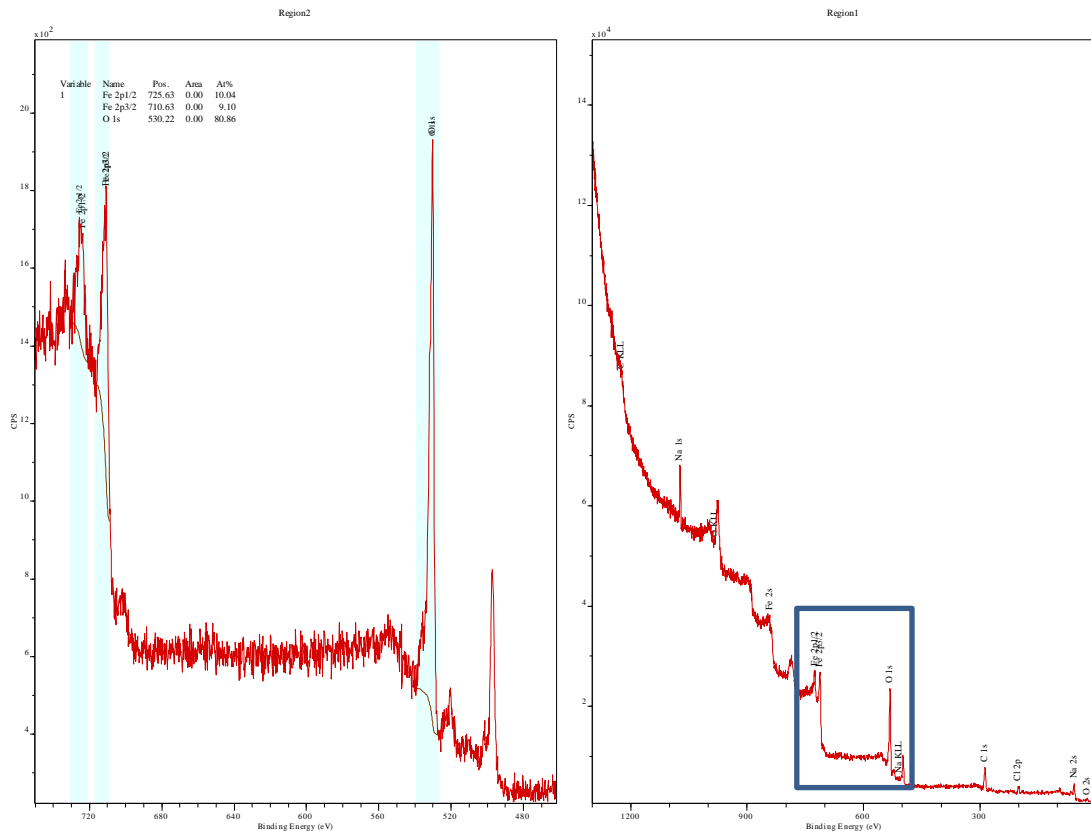
Figure 20: XPS Spectra of Iron Oxide Nanoparticles Synthesized via Co-precipitation

of the area marked by the blue rectangle in the rightmost spectrum. What we have determined from these spectra is that the samples were not thoroughly washed as they should have been. The presence of chlorine in our sample is direct evidence of insufficient wash steps. There as far as the composition is concerned, 80% of our sample consisted of oxygen were the rest is attributed to iron, carbon, sodium, and chlorine. The latter three elements are from the sodium citrate coating that was implemented on the particles. The excessive amount of oxygen in our sample is also a result of the sodium

35

citrate coating. Therefore, we cannot conclude that our particles are Fe_3O_4 and will have to utilize another characterization method in the future work.

5.4: Dynamic Light Scattering Results

All DLS measurements were taken at concentrations determined by a UV-Vis prior to sizing. Once the absorbance value of the UV-Vis spectra was found to be around 0.5, through serial dilutions, the cuvette was transferred into the DLS. The following sections each involve three graphical results from the DLS measurements with respective tables that attribute precise numerical values to the peaks seen in the graphical representations. The three graphs consist of size measurements with respect to intensity of scattered light, volume of the sample, or the measured number of particles in the sample. DLS measurements were taken only for the iron oxide nanoparticle samples, one from each method.

The gold coated iron oxide nanoparticles were not measured in the DLS for their bimetal composition would prove to result in data that was not absolutely characteristic of them. The layer of gold doesn't mimic the behavior of a solid gold nanoparticle. Also the variation in the shell thickness would contribute to misconstrued conclusions. The DLS data would be useful in an application such as measurements being taken of 3 or more samples of gold coated iron where the shell thickness were equivalent within each sample. This would allow for relative comparison among the three samples, however with one sample there is no opportunity for a relative analysis.

5.4.1: Iron Oxide Nanoparticles-Thermal Decomposition Method

Figure 21 shows the readings acquired from a measurement of size as it pertains to the measured intensity of the scattered light. As observed from the numerous peaks in

the graph there are several distinct sizes present in the sample. The most concerning value from the table is that 68.2% of the particles, by intensity, are about 207 nm in diameter. Reasons for this large value could be due to aggregation of the particles within the solution or to the presence of contaminants, remaining chemicals from the procedure, which are interfering with the scattering measurements.

	Diameter (nm)	%intensity	Width
Peak 1	207.1	68.2	14.9
Peak 2	22.9	18.4	1.65
Peak 3	5.149	13.4	0.3742
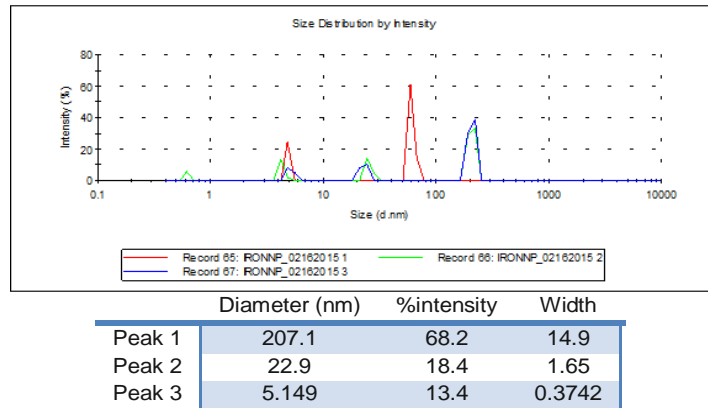
Figure 21: Intensity Readings from DLS Measurements of Iron Oxide Particles Synthesized by Thermal Decomposition

Measurements made with respect to volume show a slightly different proportion of sizes when compared to that of intensity. The peaks seen in the distribution of sizes in the volume measurement, Figure 22, show that over 98% of the particles are around 5 nm in diameter.

	Diameter (nm)	%intensity	Width
Peak 1	210.7	0.1	26.24
Peak 2	22.66	1.5	2.885
Peak 3	5.101	98.3	0.636

Figure 22: Volume Readings from DLS Measurements of Iron Oxide Particles Synthesized by Thermal Decomposition

The sizes determined by measurements made in respect to the number of particles, Figure 23, almost exactly represent the same conclusions drawn from the volume measurements. The value calculated for the size found in this measurement shows that the particles, by number, are all around 5 nm, 100%. The green peaks seen in the distribution plots in this section are all shifted to the left, smaller sizes, compared to the other two peaks. The fact that the same pattern is seen between all the distributions suggests that the device was measuring residual organics within the sample at the time. These residual organics are the oleic acid and/or oleylamine that remained after the centrifugation process.

	Diameter (nm)	%intensity	Width
Peak 1	5.037	100	0.6107

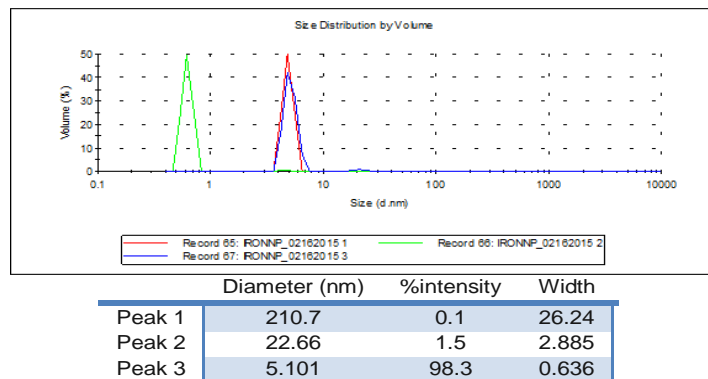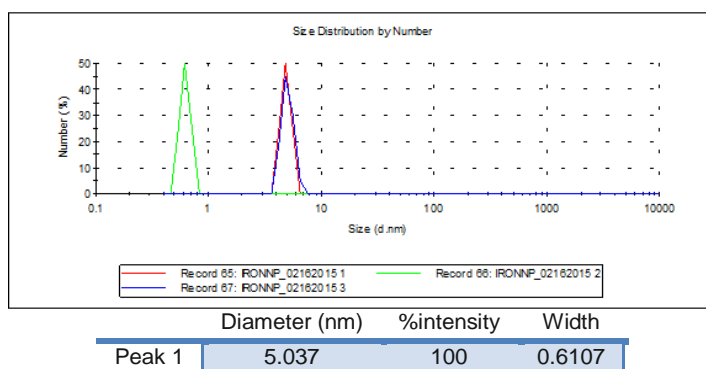**Figure 23: Number Reading from DLS Measurements of Iron Oxide Particles Synthesized by Thermal Decomposition**

5.4.2: Iron Oxide Nanoparticles-Co-Precipitation Method

The following data represents the DLS measurements for the iron oxide nanoparticles synthesized by the co-precipitation method. At first glance of the distribution of sizes in respect to intensity, Figure 24, it is seen that the particles resulting from this method are many times larger than in the previous method. The majority of the particles measured showed to be close to 200 nm (92.7%) which is actually very close to

the max peak found from the particles synthesized in the previous method, about 207 nm (68.2%).

	Diameter (nm)	%intensity	Width
Peak 1	194.4	92.7	66.18
Peak 2	64.91	5.5	10.09
Peak 3	5216	1.8	464.1
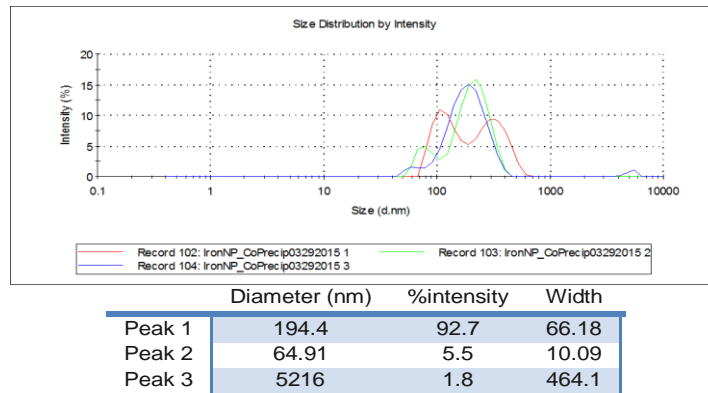
Figure 24: Intensity Readings from DLS Measurements of Iron Oxide Particles Synthesized by Co-Precipitation

In analysis of the size distribution as it pertains to volume, Figure 25, we find that the data doesn't represent a narrower distribution, such as was seen in the previous section. The data for volume correlates to the data seen in the intensity plot such that the majority of the particles sizes are measured to be about 220 nm (48.6%) and 5.3μm (42.7%). The vast difference between these two numbers and the fact that they compose 91.3% of the sample by value can only be explained as aggregation of the particles during the measurement cycles.

	Diameter (nm)	%intensity	Width
Peak 1	217.4	48.6	74.28
Peak 2	60.53	8.7	10.66
Peak 3	5320	42.7	697.8
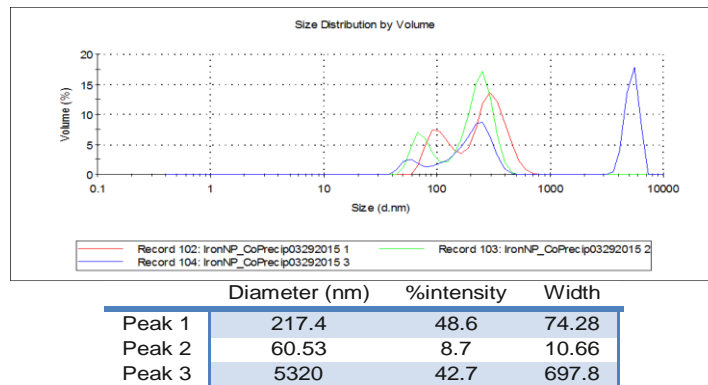
Figure 25: Volume Readings from DLS Measurements of Iron Oxide Particles Synthesized by Co=Precipitation

39

As the size distribution in respect to number of particles resulted in a 100% consensus of particle size in the previous section, the results show the same for the distribution of the co-precipitated particles, Figure 26. In the previous distributions the majority of the particles were extremely large in comparison to what is desired for possible medical applications, as previously described. The size distribution by number shows that all of the particles measured are around 73 nm in diameter. This size is smaller than the previous distributions and still a lot larger than desired but could also be a result of aggregation.

	Diameter (nm)	%intensity	Width
Peak 1	73.25	100	44.49
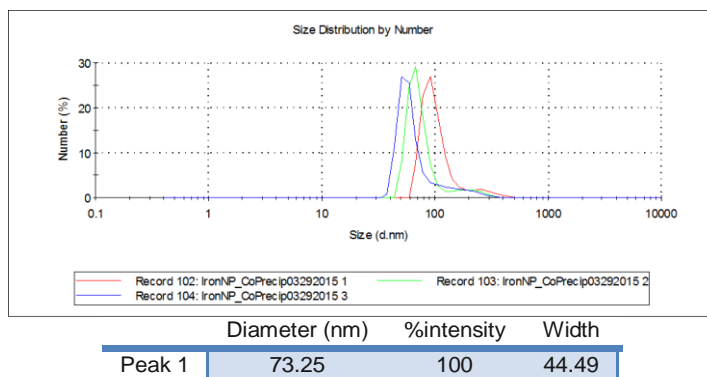
Figure 26: Number Reading from DLS Measurements of Iron Oxide Particles Synthesized by Co-Precipitation

5.4.3: Aggregation of Iron Oxide Nanoparticles

The aggregation assumption, mainly in the DLS data analysis of the co-precipitation method, has been described in literature [40] as a dependence on the balance of two opposing forces. The two forces that are partially counteracting each other are the electro static interactions of the particles and the surface tension force which correlates to surface energy of the particles, Figure 27. Even though the addition of citrate to the surface of the particles allows for dispersion in water it also creates a high energy surface that increases the chance of aggregation of particles such that the surface energy can be

reduced. It was found that in low concentrations of citrate, less bound to the surface of the particles, aggregates would form more readily [40]. Conversely, at higher citrate concentrations, meaning more citrate molecules bound to the particle surface, an increase in the electrostatic repulsion forces decreased the size of the particle aggregations within the solution [40].

Figure 27: Aggregation of Citrate Coated Iron Oxide Nanoparticles [40]
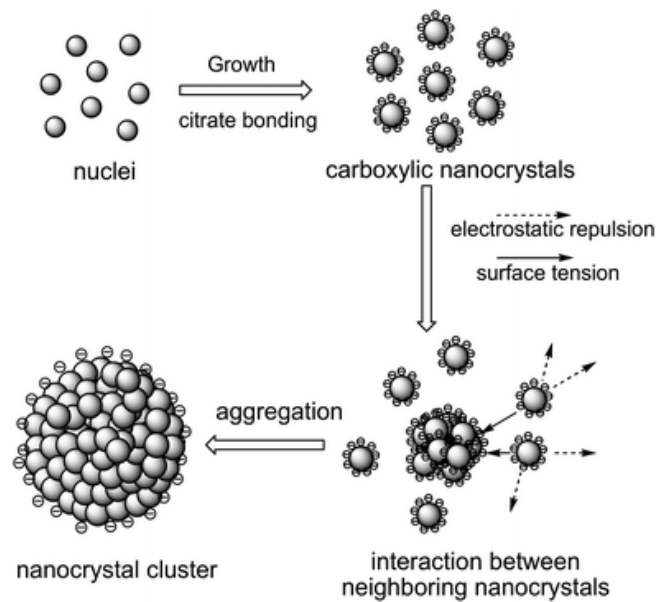
5.5: Transmission Electron Microscopy Results

The following TEM images were analyzed using ImageJ Fiji such that particle sizes could be determined through analysis of the particle widths in respect to the provided scale bar.

5.5.1: Iron Oxide Nanoparticles-Thermal Decomposition Method

The below TEM image, Figure 28, shows few individual iron oxide nanoparticles synthesized via thermal decomposition. The DLS data, analyzed previously, measured the size of these particles to be around 5 nm by the volume and number size distributions, larger by intensity (207 nm). When the image was analyzed using ImageJ Fiji, the size of the particles were found to be around 9-11nm which is about twice the size of the DLS results.
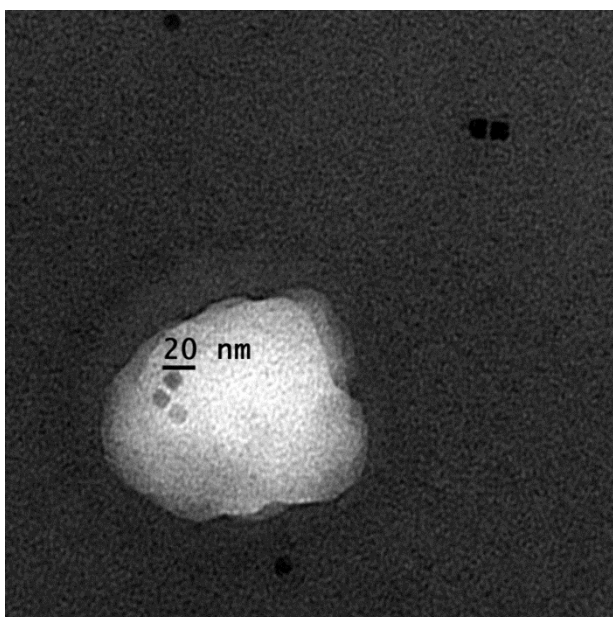
Figure 28: TEM Image of Iron Oxide Nanoparticles Synthesized via Thermal Decomposition

Seen in the image, there is a white pocket containing three particles as well as the scale bar. The dark around the rest of the image is assumed as large amounts of oleic acid and oleylamine. The few particles that can still be seen around the image were also analyzed in this size analysis. It is also interesting to notice that the shapes of the particles are more cube-like than spherical.

5.5.2: Gold Coated Iron Oxide Nanoparticles-Thermal Decomposition Method

The particles imaged below, Figure 29, show the previous particles of thermally decomposed iron particles after the gold coating procedure. As already mentioned there wasn't any DLS data taken for these gold coated particles for comparison to sizes found in the TEM results. The only idea of the sizes ahead of time is that they would be larger than 9-11 nm, the size of the iron cores from the TEM images. Through analysis of the gold coated particles image, the sizes were found to range from 7-15nm.
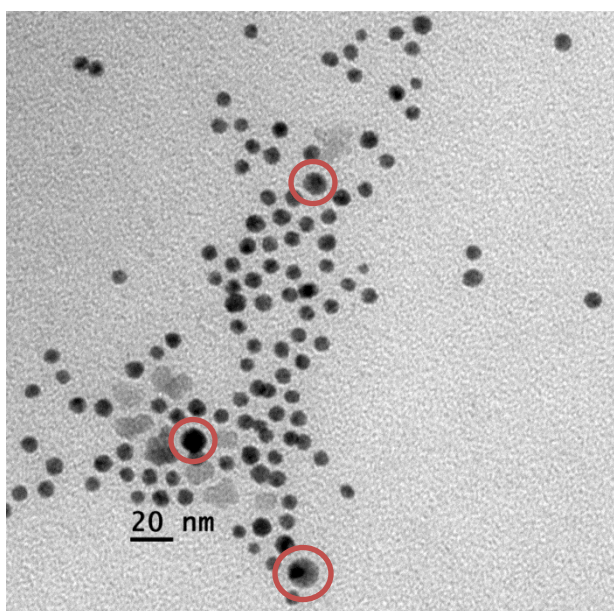
Figure 29: TEM of Gold Coated Iron Oxide Nanoparticles

Outlined in the image, with a red circle, are particles that fit the size requirements to be a 9-11 nm diameter iron oxide particle with a gold coating of 1-2 nm in thickness. The majority of the rest of the particles fall into the category of 7-8 nm in diameter uniformly. This leads to the assumption that the smaller particles are purely gold particles formed from possible excess of gold acetate during the reaction procedure. An additional reason for gold particles being in the finished result was touched upon in the centrifuge

process. There were supposed to be two pellets, different sizes dependent on shell thickness, produced from the two spins performed at different speeds. As shown, there was only a pellet from the first spin. This led us to believe that the unwanted particles, the purely gold particles, were spun into our first pellet instead of the second as desired.

5.5.3: Iron Oxide Nanoparticles-Co-Precipitation Method

All we knew about the sizes of the co-precipitated iron oxide particles, before the TEM image in Figure 30, was that the size distributions were going to be large as well as the size of the particles themselves. The DLS data measured the size to be 73 nm in diameter, the smallest value, which was given in the number distribution at 100%.
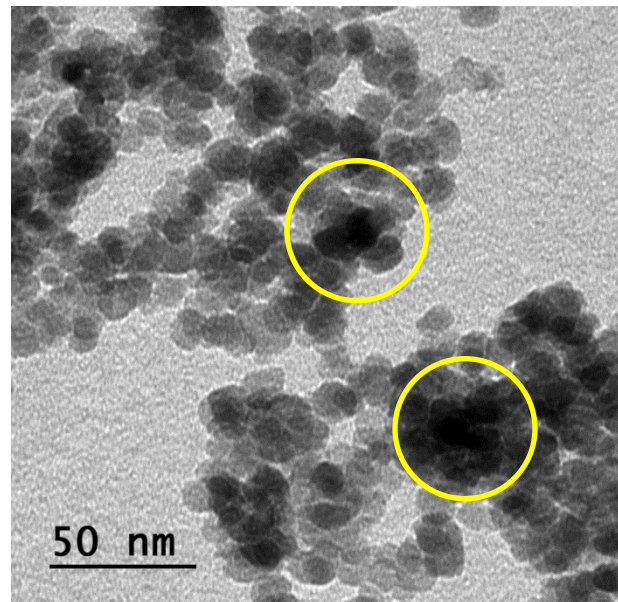
Figure 30: TEM Image of Iron Oxide Nanoparticles Synthesized via Co-Precipitation

Fortunately, the aggregation issues we assumed were correct for the image analysis found that the majority of the particles were in the range of 8-12 nm in diameter. It is clear to see that aggregation is an issue as particles seem to overlap each other in the TEM image creating the dense black portions of the image, marked with yellow circles. I

also found it interesting that with this different method of synthesis the shapes of the particles were closer to a spherical shape than those of the thermal decomposition method.

Chapter 6: Conclusions and Future Progress

The method of thermal decomposition allowed for the size distributions, from DLS measurements, to fall approximately within the desired range (Figure 23) as opposed to the co precipitation method (Figure 26). In contrast, by analyzing the TEM images it was determined that the particles from both methods were approximately the same size (Figures 28 and 30). With the UV-Vis spectra comparison we can conclude that the particles made in both methods are of similar composition (Figure 17). Comparing our acquired FTIR spectrum (Figure 18) to the literature spectrum (Figure 19) it would seem to confirm that we had created Fe_3O_4 but it would be best to have X-Ray Diffraction (XRD) data, concerning the crystal structure, for a more concrete conclusion.

For future progress in this research there would be several recommended improvements in the experimental procedures to increase the consistency and quality of our product. The experimental setup used in the iron particle synthesis procedures would be altered mainly to improve the heating and monitoring capabilities of the system. This would involve replacing the hot plate and sand/oil bath with a mantle. This change would also require an external stirring device since the hot plate utilized a magnetic stirring function. Using a mantle would allow for more consistent heating for the sand bath reflects heat back onto the hot plate surface altering the heating capabilities. A mantle would also eliminate reflected heat from a bath, allowing the reaction to reach higher temperatures and therefore larger sizes. The use of an accurate thermocouple to measure the temperature of the liquid, with little external adjustment, would also increase the efficiency of the process greatly.

The centrifugation processes for the thermal decomposition method, both iron oxide nanoparticle synthesis and the gold coating process, would be investigated for possible improvements. The purpose of this change would be an attempt to allow for better separation of the oleic acid/oleylamine excess from the bare/gold coated iron oxide nanoparticles. Changes in the gold coated centrifuge process would allow for better separation of the supposed pure gold particles from those that are gold coated iron cores.

Concerning the phase transfer of the particles synthesized by thermal decomposition; there is a possibility that the excess of oleic acid/oleylamine could be removed by proper centrifugation speeds. If adjusting the spin speeds didn't result in transferrable product more extensive experiments with various surfactants would have to be investigated. A combination of different spin speeds and surfactants, previously attempted, should be attempted once more before exploring additional surfactants.

Additional research would be conducted on the particles synthesized via co-precipitation. The area that needs to be investigated concerns the sodium citrate that is administered to assist in the particle taking a gold coating as well as particle aggregation, as previously described. The addition of more sodium citrate in either case would benefit both the acceptance of a gold coating and decrease the chance of aggregation. If the additional sodium citrate does not function in assisting the gold coating process then a different stabilizer should be investigated that also conducts the addition of gold to the surface of the iron oxide nanoparticles. The same is true for the issue of excessive aggregation, if more sodium citrate does not succeed in this scenario then another stabilizer needs to be investigated.

With these future progressions there would be potential availability of two processes for creating iron oxide nanoparticles and coating them in gold. Having these two methods provides flexibility for the steps that may follow, such as functionalization of the particles.

Works Cited

[1] "Cancer Facts & Figures," American Cancer Society, Atlanta, 2014.

[2] P. Tilman, C. Perka and H. Hommel, "Increased Accuracy of MRI-based Versus CT-based Patient Specific Instrumentation in Total Knee Arthroplasty," in *2014 AAOS Annual Meeting*, New Orleans, 2014.

[3] FDA, "FDA Drug Safety Communication: New Warnings for Using Gadolinium-based Contrast Agents in Patients with Kidney Dysfuntion," Food and Drug Administration, 2010.

[4] T. Engel, "Nuclear Magnetic Resonance Spectroscopy," in *Quantum Chemistry & Spectroscopy*, Upper Saddle River, Pearson Education Inc., 2010, pp. 407-437.

[5] A. Berger, "Magnetic Resonance Imaging," *British Medical Journal,* 2002.

[6] A. Vagal, "MRI (Magnetic Resonance Imaging) and MR Angiography," February 2013. [Online]. Available: http://www.mayfieldclinic.com/PE-MRI.htm#.VLVWgyvF8eh. [Accessed 21 October 2014].

[7] Auckland, "What is MRI?," 2006. [Online]. Available: http://atlas.scmr.org/mri.html. [Accessed 22 October 2014].

[8] W. Xing, "Introduction about CAs and relaxivity," Stony Brook University, 2012. [Online]. Available: http://mysbfiles.stonybrook.edu/~wxing/labwork_balaji_compare.html. [Accessed 13 January 2015].

[9] M. I. G. Softways, "Relaxivity," 2014-b. [Online]. Available: http://www.mr-tip.com/serv1.php?type=db1&dbs=relaxivity. [Accessed 21 October 2014].

[10] M. I. G. Softways, "Relaxation Time," 2014-a. [Online]. Available: http://www.mr-tip.com/serv1.php?type=db1&dbs=Relaxation%20Time. [Accessed 21 October 2014].

[11] H. J. Reich, "8.1 Relaxation in NMR Spectroscopy," 5 July 2014. [Online]. Available: http://www.chem.wisc.edu/areas/reich/nmr/08-tech-01-relax.htm. [Accessed 21 October 2014].

[12] M. I. G. Softways, "Gadolinium," 2014. [Online]. Available: http://www.mr-tip.com/serv1.php?type=db1&dbs=Gadolinium. [Accessed 13 January 2015].

[13] C. JM, L. B and B. B, "Gadolinium as a contrast agent for NMR," *American Journal of Neuroradiology,* pp. 1041-1042, 1983.

[14] "Gadolinium and Nephrogenic Systemic Fibrosis (NSF)," Government of Western Australia, Department of Health, July 2014. [Online]. Available: http://www.imagingpathways.health.wa.gov.au/index.php/about-imaging/diagnostic-imaging-pathways-overview-contrast-agents/gadolinium-contrast-for-mri-scans. [Accessed 13 January 2015].

[15] N. Nainani and M. Panesar, "Nephrogenic systemic fibrosis," *American Journal of Nephrology,* vol. 29, no. 1, pp. 1-9, 2009.

[16] J. Schlaudecker and C. Bernheisel, "Gadolinium-Associated Nephrogenic Systemic Fibrosis," *American Family Physician,* vol. 80, no. 7, pp. 711-714, 2009.

[17] Wahajuddin and S. Arora, "Superparamagnetic iron oxide nanoparticles: magnetic nanoplatforms as drug carriers," *International Journal of Medicine,* vol. 7, pp. 3445-3471, 2012.

[18] D. Zhu, F. Liu and L. Ma, "Nanoparticle-Based Systems for T1-Weighted Magnetic Resonance Imaging Contrast Agents," *International Journal of Molecular Sciences,* vol. 14, no. 5, pp. 10591-10607, 2013.

[19] B. Basly, D. Felder-Flesch and G. Pourroy, "Properties and suspension stability of dendronized iron oxide nanoparticles for MRI applications," *Contrast Media & Molecular Imaging,* vol. 6, pp. 132-138, 2010.

[20] S. Laurent and D. Forge, "Magnetic Iron Oxide Nanoparticles: Synthesis, Stabilization, Vectorization, Physicochemical Characterizations, and Biological Applications," *Chemical Reviews,* vol. 108, no. 6, pp. 2064-2110, 2008.

[21] H. Zhou and J.-P. Kim, "Self-Assembly Mechanism of Spiky Magnetoplasmonic Supraparticles," *Advanced Functional Materials,* vol. 24, pp. 1439-1448, 2014.

[22] S. Sun, "Monodisperse MFe2O4 (M = Fe, Co, Mn) Nanoparticles," *Journal of the American Chemical Society,* pp. 273-279, 2004.

[23] "Ultraviolet/visible spectroscopy," in *Modern Chemical Techniques*, The Royal Society of Chemistry, 1998, pp. 92-115.

[24] "SpectraSchool," Royal Society of Chemistry, 2015. [Online]. Available: http://www.rsc.org/learn-chemistry/collections/spectroscopy/introduction#IRSpectroscopy. [Accessed 17 March 2015].

[25] *Introduction to Fourier Transform Infrared Spectrometry,* Madison: Thermo Nicolet

Corporation, 2001.

[26] "XPS Works," Los Alamos National Laboratory, 2000. [Online]. Available: http://www.lanl.gov/orgs/nmt/nmtdo/AQarchive/04summer/XPS.html. [Accessed 18 March 2015].

[27] "How XPS Works," SEAL Laboratories, [Online]. Available: http://www.seallabs.com/how-xps-works.html. [Accessed 16 March 2015].

[28] "Dynamic Light Scattering: An Introduction in 30 minutes," Malvern Instruments, DLS Technical Note.

[29] "Understanding Dynamic Light Scattering," Wyatt Technology Corporation, 2014. [Online]. Available: http://www.wyatt.com/theory/theory/understanding-qels-dynamic-light-scattering.html. [Accessed 15 January 2015].

[30] "The Transmission Electron Microscope," Nobel Media AB, 2015. [Online]. Available: http://www.nobelprize.org/educational/physics/microscopes/tem/. [Accessed 18 March 2015].

[31] "Transmission Electron Microscope-A Basic Look How TEMs Work," AZoNano, 11 June 2013. [Online]. Available: http://www.azonano.com/article.aspx?ArticleID=1723. [Accessed 18 March 2015].

[32] J. Gautlier, E. Allard-Vannier and K. Herve-Aubert, "Design strategies of hybrid metallic nanoparticles for theragnostic applications," *Nanotechnology,* vol. 24, no. 43, pp. 1-14, 2013.

[33] L. Wang, "Monodispersed Core-Shell Fe3O4@Au Nanoparticles," *The Journal of Physical Chemistry,* pp. 21593-21601, 2005.

[34] Y. Wang, J. F. Wong and X. Teng, ""Pulling" Nanoparticles into Water: Phase Transfer of Oleic Acid Stabilized Monodisperse Nanoparticles into Aqueous Solutions of a-Cyclodextrin," *Nano Letters,* vol. 3, no. 11, pp. 1555-1559, 2003.

[35] Y.-J. Zhang, Y.-W. Lin and C.-C. Chang, "Magnetic properties of hydrophilic iron oxide/polyaniline nanocomposites synthesized by in situ chemical oxidative polymerization," *Synthetic Metals,* vol. 160, pp. 1086-1091, 2010.

[36] H. Hakkinen, "The gold–sulfur interface at the nanoscale," *Nature Chemistry,* vol. 4, pp. 443-455, 2012.

[37] M. C. Mascolo, Y. Pei and T. A. Ring, "Room Temperature Co-Precipitation Synthesis of

Magnetite Nanoparticles in a Large pH Window with Different Bases," *Materials,* vol. 6, pp. 5549-5567, 2013.

[38] T. T. H. Pham, C. Cao and S. J. Sim, "Application of citrate-stabilized gold-coated ferric oxide composite nanoparticles for biological separations," *Journal of Magnetism and Magnetic Materials,* vol. 320, pp. 2049-2055, 2008.

[39] G. A. El-Mahdy, A. M. Atta and H. A. Al-Lohedan, "Synthesis and Evaluation of Poly(Sodium 2-Acrylamido-2-Methylpropane Sulfonate-co-Styrene)/Magnetite Nanoparticle Composites as Corrosion Inhibitors for Steel," *Molecules,* vol. 19, no. 2, pp. 1713-1731, 2014.

[40] C. Cheng, Y. Wen, X. Xu and H. Gu, "Tunable synthesis of carboxyl-functionalized magnetite nanocrystal clusters with uniform size," *Journal of Materials Chemistry,* vol. 19, pp. 8782-8788, 2009.

[41] O. Stuart, "MRIMASTER.COM," 30 October 2014. [Online]. Available: https://mrimaster.com/. [Accessed 29 March 2015].

Appendix I: Concentration Calculations

Finding the Number of Fe Atoms per Nanoparticle:

$Fe_3O_4\ Unit\ cell\ Volume = 590.5 \cdot 10^{-24}\ cm^3$

$Average\ Nanoparticle\ Diameter = 70\ nm$

$Average\ Nanoparticle\ Volume = \frac{4}{3} \cdot \pi \cdot r^3 = \frac{4}{3} \cdot \pi \cdot (3.5 \cdot 10^{-6} cm)^3 = 1.79 \cdot 10^{-16}\ cm^3$

$Therfore\ the\ number\ of\ unit\ cells\ per\ particle\ is = \dfrac{1.79 \cdot 10^{-16}\ cm^3}{590.5 \cdot 10^{-24}\ cm^3}$

$= 303132\ \dfrac{units}{particle}$

$In\ each\ unit\ cell\ is\ 24\ Fe\ Atoms\ so: 24 \cdot 303132 = 7275168\ \dfrac{Fe\ atoms}{particle}$

Finding the Number of Fe Atoms in the Product:

$Mass\ Ratio\ of\ Fe\ in\ FeCl_3 = \dfrac{55.845\frac{g}{mol}}{3\left(35.45\frac{g}{mol}\right)} = 52.51\%$

$Mass\ Ratio\ of\ Fe\ in\ FeCl_2 = \dfrac{55.845\frac{g}{mol}}{2\left(35.45\frac{g}{mol}\right)} = 78.77\%$

$Mass\ of\ Fe\ atoms\ within\ FeCl_3\ added\ initially = 0.5251 \cdot 1.622 gm = 0.8517 gm$

$Mass\ of\ Fe\ atoms\ within\ FeCl_2\ added\ initially = 0.7877 \cdot 0.994 gm = 0.7830 gm$

$Total\ Mass\ of\ Fe\ Atoms\ in\ Reactants = 1.6347 gm$

$Total\ Moles\ of\ Fe\ Atoms\ in\ Reactants = \dfrac{1.6347 gm}{55.845\frac{gm}{mol}} = 0.02927 moles$

$Number\ of\ Fe\ Atoms\ in\ Reactants = 0.02927 moles \cdot 6.022 \cdot 10^{23}\ \dfrac{atoms}{mol}$

$= 1.76 \cdot 10^{22}\ Fe\ atoms$

Finding the Number of Nanoparticles within the Product:

$Number\ of\ Nanoparticles = \dfrac{1.76 \cdot 10^{22}\ Fe\ atoms}{7275168\frac{Fe\ atoms}{particle}} = 2.42 \cdot 10^{15}\ particles$

Finding Concentration of the Final Product:

$Concentration = \dfrac{2.42 \cdot 10^{15}\ particles}{40\ mL} \cdot \dfrac{1}{6.022 \cdot 10^{23}} \approx 1 \cdot 10^{-7} M = 0.1 \cdot 10^{-6} M = 0.1 \mu M$

Author's Bio

Nicklaus Carter was born in Blue Hill, Maine, on January 14th 1993. He was raised in Franklin, Maine, and graduated from Sumner Memorial High School in 2011. During his four years at the University of Maine Nick was enrolled as part of the Honors College, majored in Bioengineering, and attained a minor in Chemistry. In his senior year he was invited and joined the national engineering honors society, Tau Beta Pi.

Upon his graduation in May 2015, Nick plans to pursue a career in research and development where he can contribute to the medical device industry. He hopes to work in the medical device industry to enforce and expand his skills and knowledge in the industrial environment.